Rare Earth Element Yttrium Modified Mg-Al-Zn Alloy: Microstructure, Degradation Properties and Hardness

Long Liu [1,†], Fulai Yuan [2,†], Mingchun Zhao [3], Chengde Gao [1], Pei Feng [1], Youwen Yang [1], Sheng Yang [4] and Cijun Shuai [1,5,*]

[1]   State Key Laboratory of High Performance Complex Manufacturing, Central South University, Changsha 410083, China; liulong@csu.edu.cn (L.L.); gaochengde@csu.edu.cn (C.G.); fengpei@csu.edu.cn (P.F.); yangyouwen@csu.edu.cn (Y.Y.)

[2]   Health Management Center, Xiangya Hospital, Central South University, Changsha 410008, China; yuanfulai2017@csu.edu.cn

[3]   School of Material Science and Engineering, Central South University, Changsha 410083, China; mczhao@csu.edu.cn

[4]   Human Reproduction Center, Shenzhen Hospital of Hongkong University, Shenzhen 518053, China; tobyys2000@aliyun.com

[5]   Key Laboratory of Organ Injury, Aging and Regenerative Medicine of Hunan Province, Changsha 410008, China

*   Correspondence: shuai@csu.edu.cn; Tel.: +86-731-8480-5412; Fax: +86-731-8887-9044

†   These authors contributed equally to this work.

Abstract: The overly-fast degradation rates of magnesium-based alloys in the biological environment have limited their applications as biodegradable bone implants. In this study, rare earth element yttrium (Y) was introduced into AZ61 magnesium alloy (Mg-6Al-1Zn wt %) to control the degradation rate by laser rapid melting. The results showed that the degradation rate of AZ61 magnesium alloy was slowed down by adding Y. This was attributed to the reduction of $Mg_{17}Al_{12}$ phase and the formation of Al_2Y phase that has a more active potential, which decreased galvanic corrosion resulting from its coupling with the anodic matrix phase. Meanwhile, the hardness increased as Y contents increased due to the uniform distribution of the Al_2Y and $Mg_{17}Al_{12}$ phases. However, as the Y contents increased further, the formation of excessive Al_2Y phase resulted in the increasing of degradation rate and the decreasing of hardness due to its agglomeration.

Keywords: AZ61 magnesium alloy; microstructure; degradation properties; hardness

1. Introduction

Magnesium-based alloys have aroused keen attention as biodegradable bone implants due to their unique biodegradable characteristics, proper mechanical properties and favorable biocompatibility [1–6]. The widely used Mg-Al-Zn (AZ series) alloys belong to a magnesium-based alloy, which exhibits high strength and certain degradation resistance [7–10]. Nevertheless, it still needs to further enhance degradation resistance in order to have biological applications [11–13]. The rare earth elements such as neodymium (Nd), gadolinium (Gd) and yttrium (Y) have a beneficial effect in increasing degradation resistance and enhance the mechanical properties of magnesium alloys [14–18].

Many research works have been carried out on magnesium alloys with rare earth elements. Zhang et al. [19] reported that alloying cerium (Ce) could improve mechanical properties and corrosion resistance of cast Mg-4Al-based alloy. Liu et al. [20] reported that the addition of Lanthanum (La)

could enhance the corrosion properties of AM60 alloy. Yttrium (Y), a rare earth element, has hexagonal close-packed crystal structure which is the same as that of magnesium, and the atomic radius of Y (0.18 nm) is close to that of magnesium (0.16 nm) [21]. Thus, its solid solubility limit in magnesium alloys can reach up to 11.4 wt % [22]. Moreover, Y has the same standard electrochemical potential with magnesium (−2.372 V) [23,24]. Qi et al. investigated the effects of Y on the microstructure and mechanical properties of as-cast Mg-6Zn-1Mn alloy. The results showed that Y could improve its mechanical properties significantly, and the alloy with Y content of 6.09 wt % has the best mechanical properties [25]. Luo et al. studied the corrosion resistance property and the corrosion evolution of as-cast AZ91 alloy with rare earth Y. They found that the proper amount of Y addition could improve the corrosion resistance of as-cast AZ91 alloys effectively [26].

Laser rapid melting has the characteristic of rapid solidification. The cooling rate during laser melting usually reaches up to 10^5 K/s, which can inhibit grain growth and refine the grains [27]. Meanwhile, laser rapid melting can reduce the composition segregation. Furthermore, laser rapid melting is a non-equilibrium process which can increase the solid solubility of the alloy elements [28].

In this work, the AZ61 magnesium alloys (Mg-6Al-1Zn wt %) with different Y contents (0, 1, 2, 3, 4 wt %) were prepared using laser rapid melting. The microstructure was studied by optical microscopy (OM), X-ray diffraction (XRD) and scanning electron microscopy (SEM) with energy dispersed spectroscopy (EDS). The degradation properties were analyzed by the immersion experiments. In addition, the hardness was measured by Vickers hardness tests.

2. Results and Discussion

2.1. Microstructure

The microstructures of the AZ61 magnesium alloys with different amounts of Y added were examined by optical microscopy (Figure 1) and scanning electron microscopy (Figure 2) respectively. AZ61 magnesium alloy consisted of the magnesium matrix and network precipitates (pointed by black arrows) which were distributed mainly at grain boundaries (Figures 1a and 2a). After adding Y, the network precipitates decreased and a small amount of granulous precipitates (pointed by black arrows with a round tail) appeared (Figures 1b and 2b). The granulous precipitates increased as the Y contents increased and were distributed uniformly as Y reached 2 wt % (Figures 1c and 2c). However, as the Y contents further increased, the granulous precipitates tended to be predominant and agglomerate (Figures 1d,e and 2d,e).
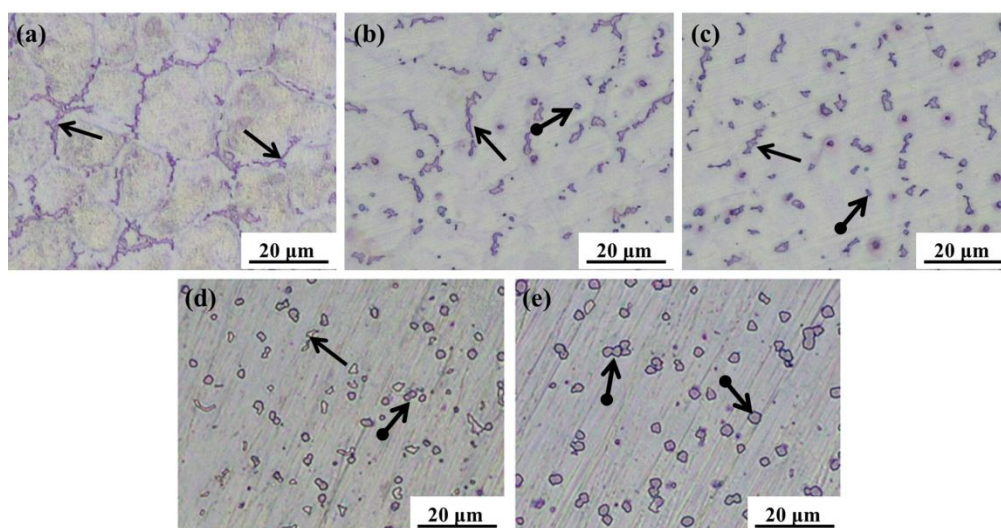

Figure 1. Optical micrographs of AZ61 magnesium alloys with different Y contents: (**a**) 0 wt %; (**b**) 1 wt %; (**c**) 2 wt %; (**d**) 3 wt % and (**e**) 4 wt %.
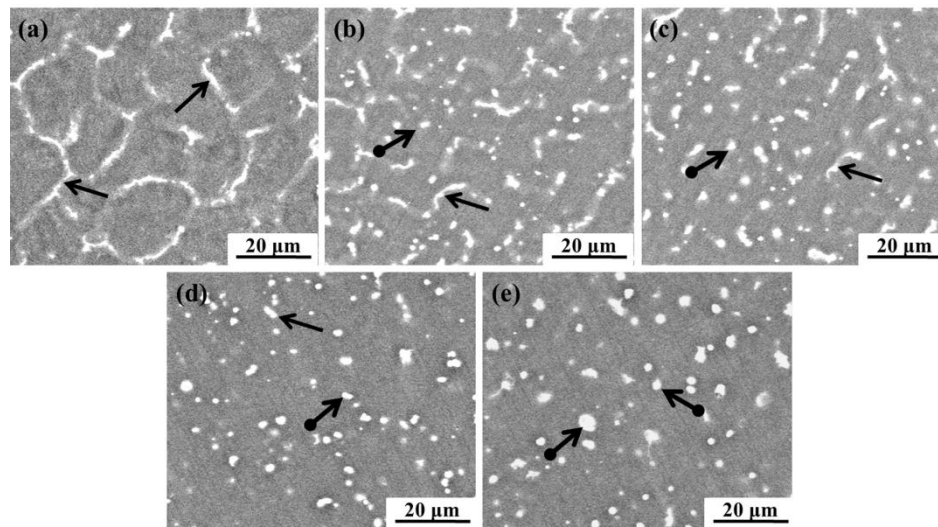
Figure 2. SEM micrographs of AZ61 magnesium alloys with different Y contents: (**a**) 0 wt %; (**b**) 1 wt %; (**c**) 2 wt %; (**d**) 3 wt % and (**e**) 4 wt %.

The XRD patterns of the AZ61 magnesium alloys with different Y contents were exhibited in Figure 3. Only the α-Mg and $Mg_{17}Al_{12}$ phase were detected in the AZ61 magnesium alloy (Figure 3a). After adding Y, a new Al_2Y phase was formed and the corresponding peak intensity gradually increased as Y increased. Meanwhile, the peak intensity of the $Mg_{17}Al_{12}$ phase decreased. This implied the reduction of the $Mg_{17}Al_{12}$ phase and the increase of the Al_2Y phase. Reference intensity ratio (RIR) method was used to quantify the weight percent of the $Mg_{17}Al_{12}$ phase and Al_2Y phase. A more complete view on the weight percent of the $Mg_{17}Al_{12}$ phase and Al_2Y phase as influenced by Y content was given in Figure 4. It could be observed that the weight percent of the $Mg_{17}Al_{12}$ phase decreased from 7.5% in the AZ61 magnesium alloy to 4.1% in the AZ61 magnesium alloy with 4 wt % Y, while that of Al_2Y increased from 0% in the AZ61 magnesium alloy to 2.5% in the AZ61 magnesium alloy with 4 wt % Y. In general, the tendency of elements to form stable compounds was in positive correlation with the electronegativity difference between elements. The electronegativity values of Y, Mg and Al were 1.22, 1.31 and 1.61 respectively, from which it could be deduced that Y was prone to react with Al to form Al-Y compound [29]. Thus, the Al_2Y phase increased gradually as Y increased, while the $Mg_{17}Al_{12}$ phase decreased.

The morphology and compositions of the second phases in AZ61 magnesium alloy with 2 wt % Y were studied by EDS. It was presented that magnesium content reduced while Al and Y increased across the granulous particles (Figure 5b). Thus, it was reasonable to conclude that the granulous particle was in the Al_2Y phase. Meanwhile, the rod-shaped phase had a Mg/Al ratio (78.78/21.22) (Figure 5c) which was close to that of $Mg_{17}Al_{12}$, and was thereby identified as $Mg_{17}Al_{12}$ phase.

The three phases (α-Mg, Al_2Y and $Mg_{17}Al_{12}$) were exactly determined in the AZ61 magnesium alloy with Y. The schematic diagram of the phase formation in the alloy was shown in Figure 6. The first precipitated phase in the solidification of the high-temperature liquid phase was the Al_2Y phase. This could be explained by the Al_2Y phase having the highest melting point (1485 °C) among the three phases (Figure 6b) [30]. Afterwards, the α-Mg phase with the melting point of 650 °C started nucleation (Figure 6c). Then, the remained Al atoms precipitated in $Mg_{17}Al_{12}$ (437 °C) which distributed on the α-Mg grain boundaries (Figure 6d).
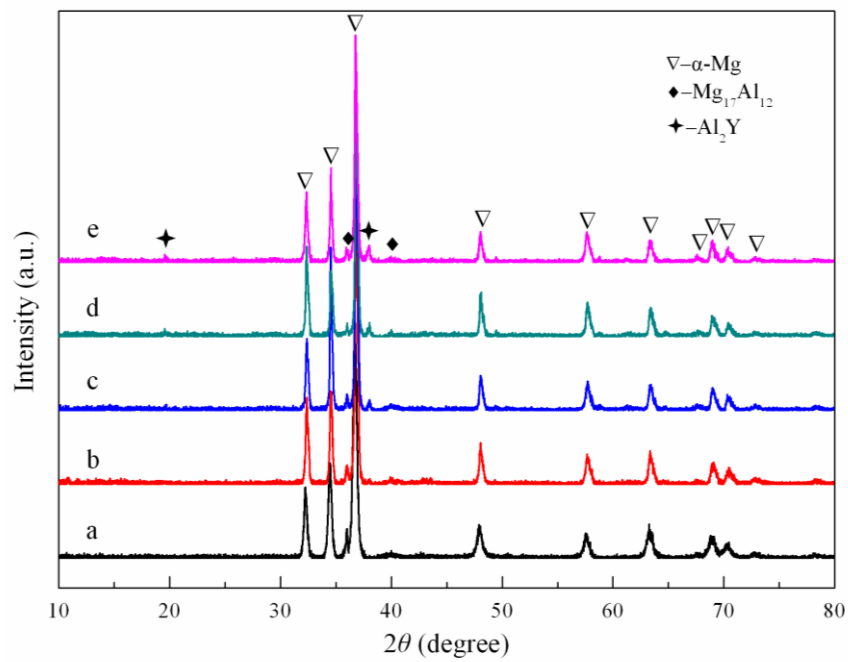
Figure 3. X-ray diffraction (XRD) patterns of AZ61 magnesium alloys with different Y contents: (**a**) 0 wt %; (**b**) 1 wt %; (**c**) 2 wt %; (**d**) 3 wt % and (**e**) 4 wt %.
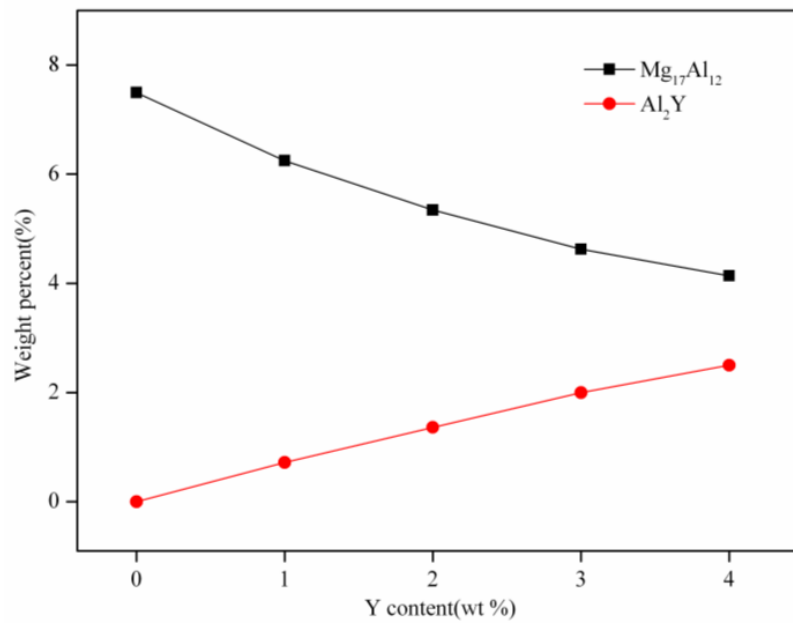

Figure 4. The weight percent of $Mg_{17}Al_{12}$ and Al_2Y phases in AZ61 magnesium alloys with Y addition.
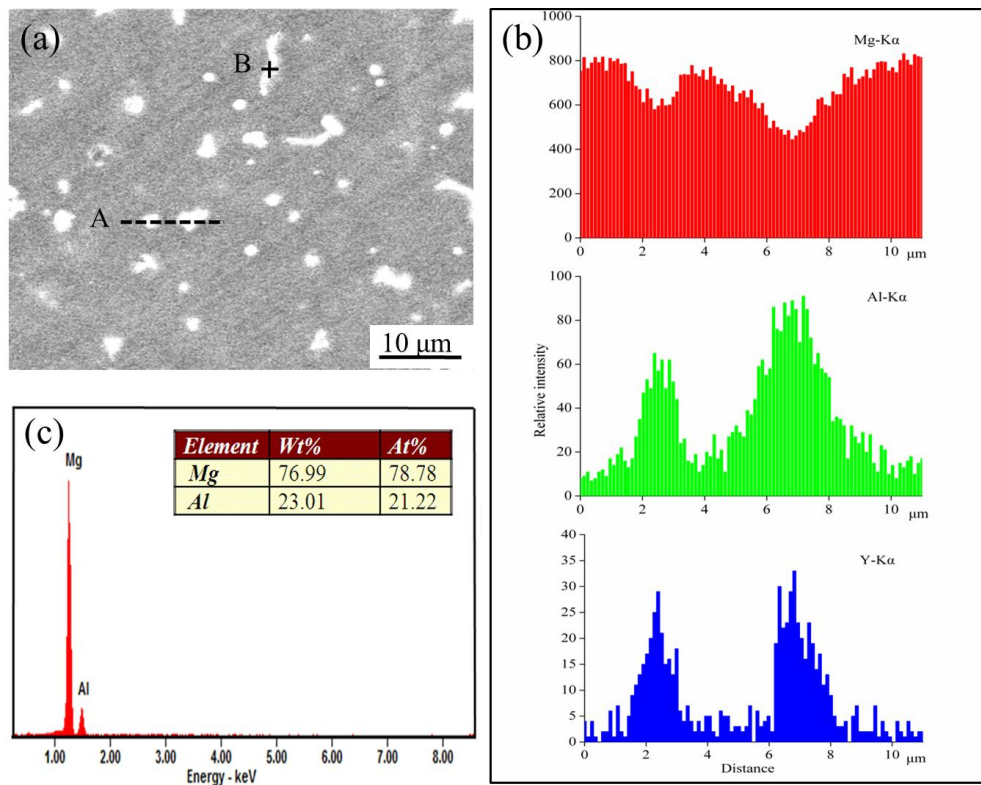
Figure 5. SEM image of (**a**) AZ61 magnesium alloy with 2 wt % Y and energy dispersive spectroscopy (EDS) patterns of (**b**) A line and (**c**) B point in (**a**).
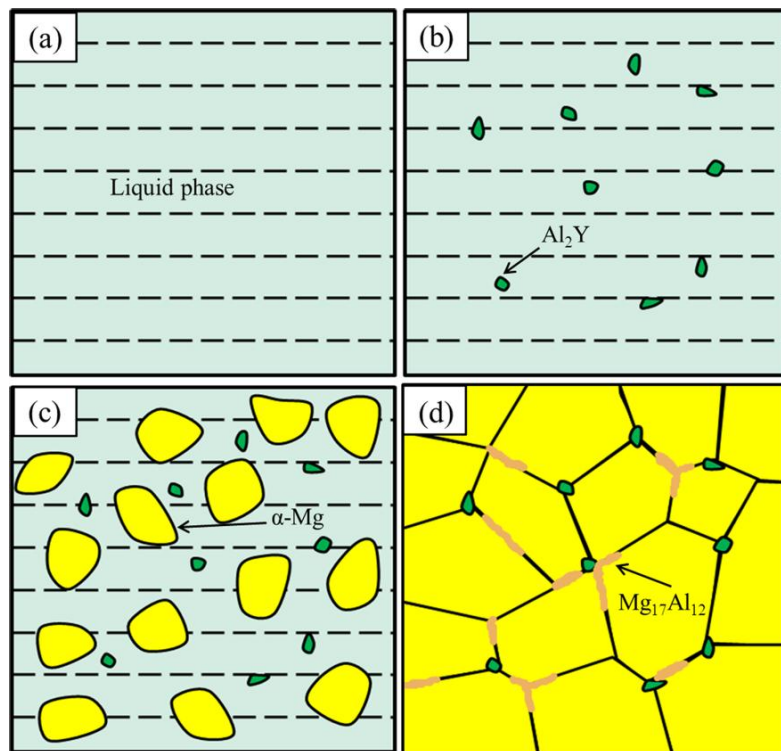

Figure 6. Schematic diagram of phase formation in the AZ61 magnesium alloy with Y (**a**) liquid phase; (**b**) Al_2Y phase precipitation; (**c**) α-Mg nucleation; (**d**) $Mg_{17}Al_{12}$ formation.

2.2. Hardness

The hardness of AZ61 magnesium alloys with different Y contents was shown in Figure 7. The hardness of AZ61 magnesium alloy was 90.9 Hv. The hardness continuously increased as Y increased from 0 wt % to 2 wt %. The optimal hardness was 104.9 Hv when the Y content was 2 wt %. However, it decreased as the Y contents further decreased. The increase of hardness was attributed to the uniform distribution of Al_2Y and $Mg_{17}Al_{12}$ phases which acted as a second phase strengthening agent in the alloy matrix. As the Y contents further decreased, the excessive Al_2Y phase formed in the alloy tended to aggregate. Thus, the structure of the alloy became uneven and the hardness of the alloy decreased.
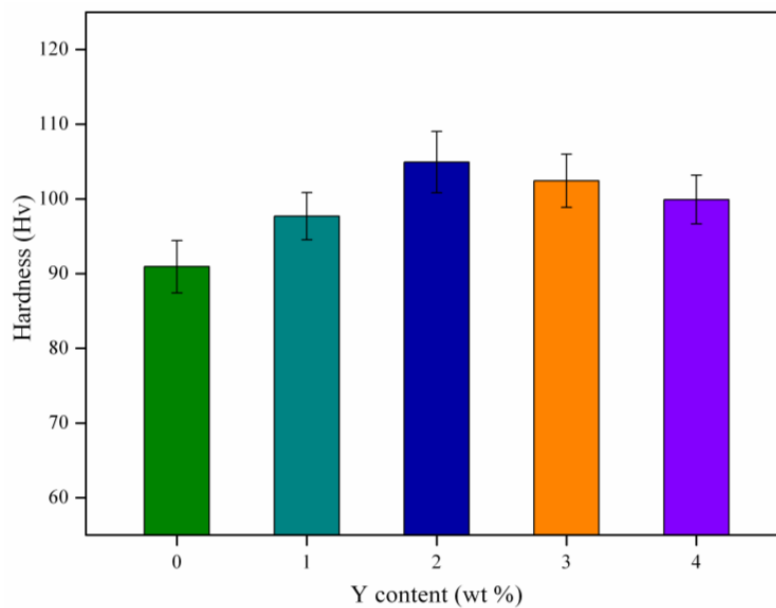

Figure 7. Hardness of AZ61 magnesium alloys with different Y contents.

2.3. Degradation Properties

Immersion tests were applied to study the degradation properties of AZ61 magnesium alloys with different Y contents. The hydrogen evolution volume varied with the immersion time, as shown in Figure 8. The hydrogen evolution volume of the alloys increased rapidly in the early stages of immersion and then increased slowly, which indicated a reduction of degradation rate. The hydrogen evolution volume of AZ61 magnesium alloys with Y contents of 0, 1, 2, 3 and 4 wt % were 30.1 mL/cm^2, 13.3 mL/cm^2, 6.1 mL/cm^2, 10.5 mL/cm^2 and 18.1 mL/cm^2 after immersion for 360 h, respectively. It was observed that the degradation rate reduced remarkably with adding Y up to 2 wt %, while a further increase of Y resulted in an increased degradation rate. The degradation rates of the AZ61 magnesium alloys with different Y contents were calculated according to mass loss test (Figure 9). The results were consistent with that of hydrogen evolution analysis, which showed that AZ61 magnesium alloy with 2 wt % Y exhibited the lowest degradation rate (0.28 mm/year). The degradation rate of AZ61 magnesium alloy with 2 wt % Y was lower than the reported value of WE43 magnesium alloy (0.85 mm/year) [31].
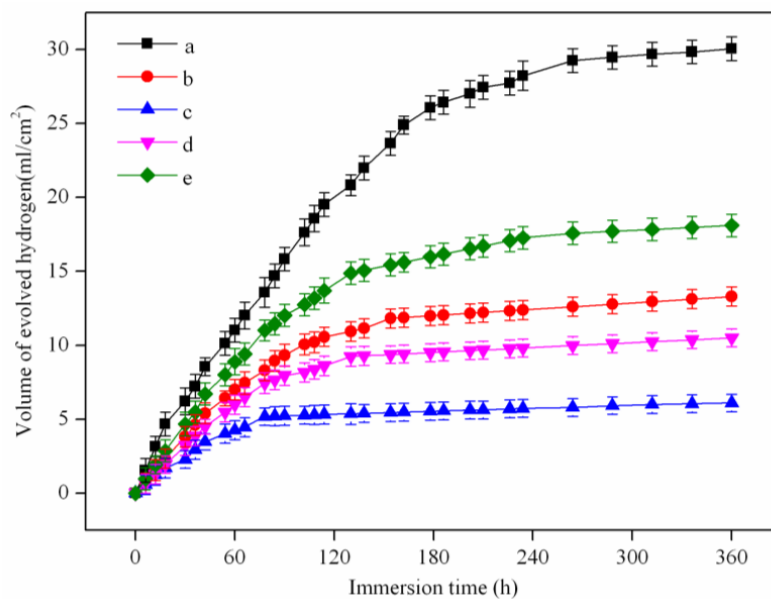
Figure 8. The hydrogen evolution volume of AZ61 magnesium alloys with different Y contents immersed in the simulated body fluid (SBF) for 360 h: (**a**) 0 wt %; (**b**) 1 wt %; (**c**) 2 wt %; (**d**) 3 wt % and (**e**) 4 wt %.
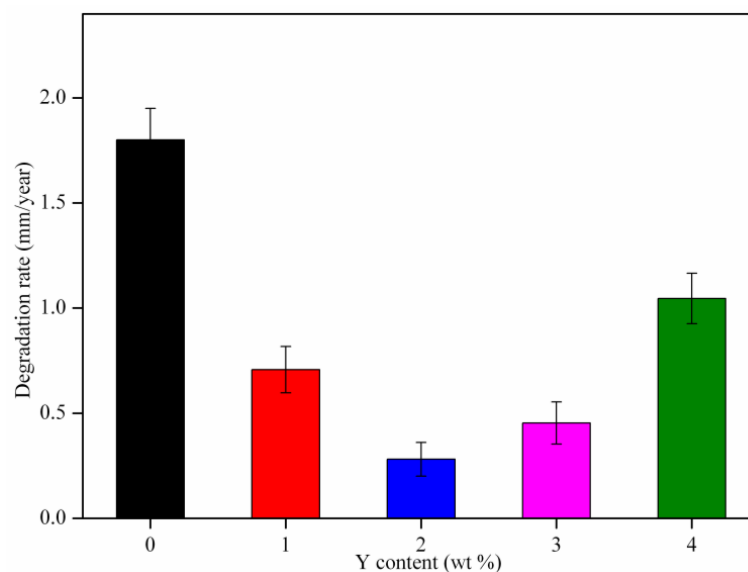

Figure 9. Degradation rates of AZ61 magnesium alloys with different Y contents after immersion in SBF solution for 7 days.

The degradation morphology of the AZ61 magnesium alloys with different Y contents after immersion for 120 h was shown in Figure 10. Obviously, the alloys were covered with a degradation product film which presented some cracks. The appearance of cracks was believed to be caused by the dehydration of the degradation product film after drying in ambient atmosphere. The AZ61 magnesium alloy exhibited a severely corroded surface with many cracks (Figure 10a). After adding 1 wt % Y, the surface of the alloy presented relatively shallow cracks. When the Y contents was 2 wt %, the integrated degradation film without a crack formed, which implied that the degradation degree of the alloy was relatively low (Figure 10c). As the Y contents further increased, the cracks of the degradation product film gradually increased (Figure 10d,e).
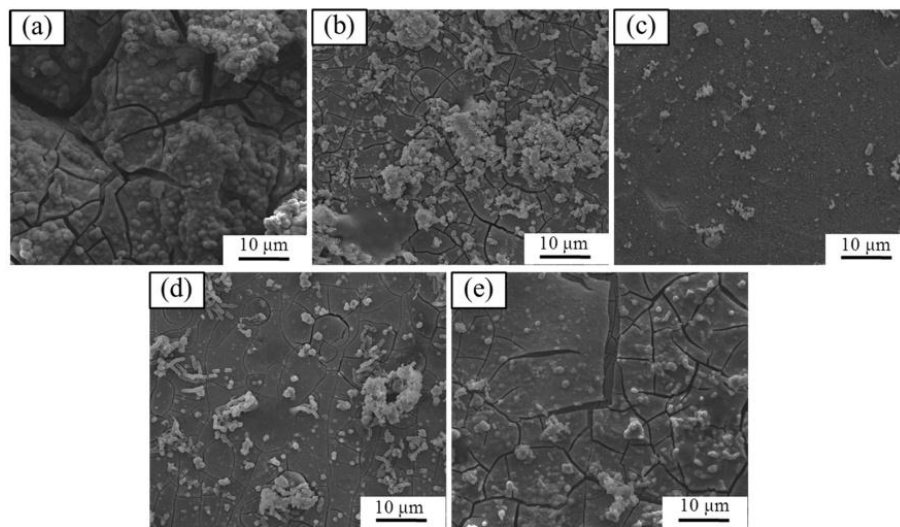
Figure 10. SEM degradation morphology of AZ61 magnesium alloys with different Y contents after immersion for 120 h: (**a**) 0 wt %; (**b**) 1 wt %; (**c**) 2 wt %; (**d**) 3 wt % and (**e**) 4 wt %.

It could be concluded that the appropriate addition of rare earth element Y could enhance degradation resistance of the AZ61 magnesium alloy. In general, the $Mg_{17}Al_{12}$ phase acted as the cathode with respect to the magnesium matrix, which facilitated the degradation of the AZ61 magnesium alloy [32]. After adding Y, Y reacted with Al to form the Al_2Y phase, which reduced the amount of $Mg_{17}Al_{12}$ phase on the grain boundaries. Furthermore, the Al_2Y phase has more active potential [33]. Thus, adding Y could suppress the galvanic corrosion of the alloys, which enhanced the degradation resistance. However, as the Y contents further increased, the excessive Al_2Y phase accelerated galvanic corrosion, resulting in the increase of degradation rate.

3. Experimental Procedure

3.1. Materials Preparation

The spherical AZ61 magnesium alloy powders were purchased from Tangshan Weihao Materials Co., Ltd. (Tangshan, China, average particle size 70 μm) and irregular-shaped Y powders were obtained from Shanghai Naiou Nano technology Co., Ltd. (Shanghai, China, average particle size 20 μm). The powder mixtures with different Y contents (0, 1, 2, 3 and 4 wt %) were prepared through ball milling in a mixed gas environment (1 vol % SF_6 and 99 vol % CO_2). The rotation speed was fixed at 450 rpm (revolution per minute) in the course of ball milling and the milling time was 2 h.

The AZ61 magnesium alloys with different Y contents (0, 1, 2, 3, 4 wt %) were prepared using a homemade laser rapid melting system. It consists of a fiber laser, a focus system, a gas protection device and a computer control system. The fiber laser has a maximum output power of 110 W. The minimum spot diameter of the laser beams is 50 μm. More details of the system are available in the reference [34]. The processing parameters were as follows: laser scanning rate 200 mm/min, laser spot 150 μm and laser power 80 W. The powder mixtures were melted layer by layer in the sealed building chamber protected by argon gas. Then, the samples of alloys (10 mm × 10 mm × 5 mm) were built up.

3.2. Materials Characterization

The prepared alloy specimens were ground with abrasive papers grading from 1000 to 2000 grit and mechanically polished on cotton cloth with 0.5 μm diamond paste, followed by being etched for 10 s with the acetic picral solution (10 mL of acetic acid, 70 mL of ethanol (99.8% *v/v*), 4.2 g of picric acid, and 10 mL of distilled water), then the metallurgical structure of alloys was studied by an optical microscopy (OM, Olympus BHM, Osaka, Japan). The composition distribution of the alloys

was studied using scanning electron microscopy (SEM, QUANTA FEG250, FEI Company, Hillsboro, OR, USA) and energy dispersive spectroscopy (EDS, JSM-5910LV, JEOL, Tokyo, Japan). The phase compositions were analyzed through X-ray diffraction (XRD, D8 Advance, Bruker Inc., Karlsruhe, Germany) using Cu-Kα radiation at 15 mA and 30 kV with scattering angles ranging from 10° to 80°, step size 0.02° and scanning speed 8°/min. X-ray diffraction patterns were identified by comparing the diffraction patterns with the standard ICDD-PDF cards. The quantitative phase analysis was conducted by means of the reference intensity ratio method [35].

Vickers hardness tests were performed by a Vickers microindenter (HXD-1000TM/LCD, Digital Micro Hardness Tester, Shanghai Taiming Optical Instrument Co. Ltd, Shanghai, China) with a load of 2.45 N and loading time of 15 s. Ten indents were made for each sample. The hardness was expressed as a mean and standard deviation of these 10 readings. The dimensions of alloys used for the immersion tests were 10 mm × 10 mm × 5 mm. Immersion tests were operated at 37 $\pm$ 0.5 °C in simulated body fluid (SBF) (the ratio of the surface area to solution volume was 1 cm^2:100 mL). The SBF that has similar ion concentrations to those of human blood plasma was prepared according to the protocol described by Kokubo et al. [36]. In short, the relevant reagent grade chemicals ($CaCl_2$, $K_2HPO_4 \cdot 3H_2O$, KCl, NaCl, $MgCl_2 \cdot 6H_2O$, $NaHCO_3$ and Na_2SO_4) were dissolved in distilled water at the appropriate amounts. The pH of the solution was buffered to physiological pH (pH = 7.4) by adding tri-hydroxymethyl-aminomethane and hydrochloric acid. The hydrogen evolution volume was monitored during the immersion. After immersion for 7 days, each sample was removed from the solution and washed with distilled water. A chromic acid solution (200 g/L Cr_2O_3 + 10 g/L $AgNO_3$) was used to remove the degradation products on the sample surface before mass loss measurement. Five samples were measured for each group to obtain reproducible results. The degradation rates (mm/year) were calculated according to mass loss test. After immersion for 120 h, the samples were taken out from SBF and then blown dry with air at room temperature. The degraded surfaces were observed by SEM. Before the SEM observations, the samples were coated with gold by using a sputter coater (Leica EM SCD005, Leica Microsystems GmbH, Wetzlar, Germany).

3.3. Statistical Analysis

The experimental data of mechanical and degradation properties were expressed as mean $\pm$ standard deviation. Statistical analysis was performed to assess the difference by the analysis of variance. The difference was considered to be significant when $p < 0.05$.

4. Conclusions

The microstructure, degradation properties and hardness of the AZ61 magnesium alloys with different Y contents (0, 1, 2, 3, 4 wt %) prepared by laser rapid melting were investigated. Adding Y to AZ61 magnesium alloy could lead to the formation of Al_2Y phase and reduce the amount of $Mg_{17}Al_{12}$ phase. The degradation resistance of the AZ61 magnesium alloy was enhanced with Y addition. The AZ61 magnesium alloy with 2 wt % Y exhibited an optimal degradation resistance. Furthermore, the hardness increased as Y contents increased from 0 wt % to 2 wt %, and then decreased when Y contents decreased further. In conclusion, laser rapid melting AZ61 magnesium alloy with 2 wt % Y exhibit prospects for future bone implants.

Author Contributions: Long Liu, Fulai Yuan and Cijun Shuai conceived and designed the experiments; Long Liu, Chengde Gao and Youwen Yang performed the experiments; Pei Feng and Sheng Yang analyzed the data;

Mingchun Zhao contributed analysis tools; Long Liu and Fulai Yuan wrote the paper. All authors reviewed the final manuscript.

Conflicts of Interest: The authors declare no conflict of interest.

References

1. Doležal, P.; Zapletal, J.; Fintová, S.; Trojanová, Z.; Greger, M.; Roupcová, P.; Podrábský, T. Influence of processing techniques on microstructure and mechanical properties of a biodegradable Mg-3Zn-2Ca alloy. *Materials* **2016**, *9*, 880–894. [CrossRef]

2. Razavi, M.; Fathi, M.H.; Meratian, M. Fabrication and characterization of magnesium-fluorapatite nanocomposite for biomedical applications. *Mater. Charact.* **2010**, *61*, 1363–1370. [CrossRef]

3. Shuai, C.; Yang, Y.; Wu, P.; Lin, X.; Liu, Y.; Zhou, Y.; Feng, P.; Liu, X.; Peng, S. Laser rapid solidification improves corrosion behavior of Mg-Zn-Zr alloy. *J. Alloy. Compd.* **2017**, *691*, 961–969. [CrossRef]

4. Tkacz, J.; Minda, J.; Fintová, S.; Wasserbauer, J. Comparison of electrochemical methods for the evaluation of cast AZ91 magnesium alloy. *Materials* **2016**, *9*, 925–938. [CrossRef]

5. Anawati, A.; Asoh, H.; Ono, S. Effects of alloying element Ca on the corrosion behavior and bioactivity of anodic films formed on AM60 Mg alloys. *Materials* **2016**, *10*, 11–26. [CrossRef]

6. Nidadavolu, E.; Feyerabend, F.; Ebel, T.; Willumeitrömer, R.; Dahms, M. On the determination of magnesium degradation rates under physiological conditions. *Materials* **2016**, *9*, 627–636. [CrossRef]

7. Niknejad, S.; Liu, L.; Lee, M.Y.; Esmaeili, S.; Zhou, N.Y. Resistance spot welding of AZ series magnesium alloys: Effects of aluminum content on microstructure and mechanical properties. *Mat. Sci. Eng. A* **2014**, *618*, 323–334. [CrossRef]

8. Guo, J.; Zhou, Y.; Liu, C.; Wu, Q.; Chen, X.; Lu, J. Wire Arc Additive manufacturing of AZ31 magnesium alloy: grain refinement by adjusting pulse frequency. *Materials* **2016**, *9*, 823–835. [CrossRef]

9. Song, W.; Martin, H.J.; Hicks, A.; Seely, D.; Walton, C.A.; Ii, W.B.L.; Wang, P.T.; Horstemeyer, M.F. Corrosion behaviour of extruded AM30 magnesium alloy under salt-spray and immersion environments. *Corros. Sci.* **2014**, *78*, 353–368. [CrossRef]

10. Jain, V.; Mishra, R.S. Superplastic behavior and microstructural stability of friction stir processed AZ91C alloy. *J. Mater. Sci.* **2013**, *48*, 2635–2646. [CrossRef]

11. Yu, W.; Zhao, H.; Ding, Z.; Zhang, Z.; Sun, B.; Shen, J.; Chen, S.; Zhang, B.; Yang, K.; Liu, M. In vitro and in vivo evaluation of MgF_2 coated AZ31 magnesium alloy porous scaffolds for bone regeneration. *Coll. Surf. B: Biointerfaces* **2017**, *149*, 330–340. [CrossRef] [PubMed]

12. Sun, W.; Zhang, G.; Tan, L.; Yang, K.; Ai, H. The fluoride coated AZ31B magnesium alloy improves corrosion resistance and stimulates bone formation in rabbit model. *Mat. Sci. Eng. C* **2016**, *63*, 506–511. [CrossRef] [PubMed]

13. Abidin, N.I.Z.; Martin, D.; Atrens, A. Corrosion of high purity Mg, AZ91, ZE41 and Mg2Zn0.2Mn in Hank's solution at room temperature. *Corros. Sci.* **2011**, *53*, 862–872. [CrossRef]

14. Cao, G.; Zhang, D.; Zhang, W.; Zhang, W. In vitro corrosion study of friction stir processed WE43 magnesium alloy in a simulated body fluid. *Materials* **2016**, *9*, 542–556. [CrossRef]

15. Stulikova, I.; Smola, B. Mechanical properties and phase composition of potential biodegradable Mg-Zn-Mn-base alloys with addition of rare earth elements. *Mater. Charact.* **2010**, *61*, 952–958. [CrossRef]

16. Levy, G.; Aghion, E. Effect of diffusion coating of Nd on the corrosion resistance of biodegradable Mg implants in simulated physiological electrolyte. *Acta Biomater.* **2013**, *9*, 8624–8630. [CrossRef] [PubMed]

17. Srinivasan, A.; Huang, Y.; Mendis, C.L.; Blawert, C.; Kainer, K.U.; Hort, N. Investigations on microstructures, mechanical and corrosion properties of Mg-Gd-Zn alloys. *Mat. Sci. Eng. A* **2014**, *595*, 224–234. [CrossRef]

18. He, W.; Zhang, E.; Yang, K. Effect of Y on the bio-corrosion behavior of extruded Mg-Zn-Mn alloy in Hank's solution. *Mat. Sci. Eng. C* **2010**, *30*, 167–174. [CrossRef]

19. Zhang, J.; Leng, Z.; Zhang, M.; Meng, J.; Wu, R. Effect of Ce on microstructure, mechanical properties and corrosion behavior of high-pressure die-cast Mg-4Al-based alloy. *J. Alloy. Compd.* **2011**, *509*, 1069–1078. [CrossRef]

20. Liu, W.; Cao, F.; Chang, L.; Zhang, Z.; Zhang, J. Effect of rare earth element Ce and La on corrosion behavior of AM60 magnesium alloy. *Corros. Sci.* **2009**, *51*, 1334–1343. [CrossRef]

21. Peng, Q.; Meng, J.; Li, Y.; Huang, Y.; Hort, N. Effect of yttrium addition on lattice parameter, Young's modulus and vacancy of magnesium. *Mat. Sci. Eng. A* **2011**, *528*, 2106–2109. [CrossRef]

22. Xin, Y.; Hu, T.; Chu, P.K. In vitro studies of biomedical magnesium alloys in a simulated physiological environment: a review. *Acta Biomater.* **2011**, *7*, 1452–1459. [CrossRef] [PubMed]

23. Liu, M.; Schmutz, P.; Uggowitzer, P.J.; Song, G.; Atrens, A. The influence of yttrium (Y) on the corrosion of Mg-Y binary alloys. *Corros. Sci.* **2010**, *52*, 3687–3701. [CrossRef]

24. Vlček, M.; Lukáč, F.; Kudrnová, H.; Smola, B.; Stulíková, I.; Luczak, M.; Szakács, G.; Hort, N.; Willumeit-Römer, R. Microhardness and in vitro corrosion of heat-treated Mg–Y–Ag biodegradable alloy. *Materials* **2017**, *10*, 55–66. [CrossRef]

25. Qi, F.; Zhang, D.; Zhang, X.; Pan, F. Effect of Y addition on microstructure and mechanical properties of Mg-Zn-Mn alloy. *Trans. Nonferr. Metal. Soc. China* **2014**, *24*, 1352–1364. [CrossRef]

26. Luo, T.; Yang, Y. Corrosion properties and corrosion evolution of as-cast AZ91 alloy with rare earth yttrium. *Mater. Des.* **2011**, *32*, 5043–5048. [CrossRef]

27. Xie, D.; Zhao, J.; Qi, Y.; Yue, L.; Shen, L.; Xiao, M. Decreasing pores in a laser cladding layer with pulsed current. *Chin. Opt. Lett.* **2013**, *11*, 54–57.

28. Wei, K.; Gao, M.; Wang, Z.; Zeng, X. Effect of energy input on formability, microstructure and mechanical properties of selective laser melted AZ91D magnesium alloy. *Mater. Sci. Eng. A* **2014**, *611*, 212–222. [CrossRef]

29. Zhao, J.; Zhang, J.; Liu, W.; Wu, G.; Zhang, L. Effect of Y content on microstructure and mechanical properties of as-cast Mg-8Li-3Al-2Zn alloy with duplex structure. *Mat. Sci. Eng. A* **2016**, *650*, 240–247. [CrossRef]

30. Dai, J.; Zhu, S.; Easton, M.A.; Zhang, M.; Qiu, D.; Wu, G.; Liu, W.; Ding, W. Heat treatment, microstructure and mechanical properties of a Mg-Gd-Y alloy grain-refined by Al additions. *Mat. Sci. Eng. A* **2013**, *576*, 298–305. [CrossRef]

31. Wang, C.; Yu, Z.; Cui, Y.; Zhang, Y.; Yu, S.; Qu, G.; Gong, H. Processing of a novel Zn alloy micro-tube for biodegradable vascular stent application. *J. Mater. Sci. Technol.* **2016**, *32*, 925–929. [CrossRef]

32. Zhou, W.; Shen, T.; Aung, N.N. Effect of heat treatment on corrosion behaviour of magnesium alloy AZ91D in simulated body fluid. *Corros. Sci.* **2010**, *52*, 1035–1041. [CrossRef]

33. Zhang, J.; Wang, J.; Qiu, X.; Zhang, D.; Zheng, T.; Niu, X.; Tang, D.; Meng, J. Effect of Nd on the microstructure, mechanical properties and corrosion behavior of die-cast Mg-4Al-based alloy. *J. Alloy. Compd.* **2008**, *509*, 1069–1078. [CrossRef]

34. Yang, Y.; Wu, P.; Lin, X.; Liu, Y.; Bian, H.; Zhou, Y.; Gao, C.; Shuai, C. System development, formability quality and microstructure evolution of selective laser-melted magnesium. *Virtual Phys. Prototyp.* **2016**, *11*, 1–9. [CrossRef]

35. Gao, C.; Wei, P.; Feng, P.; Xiao, T.; Shuai, C.; Peng, S. Nano SiO_2 and MgO improve the properties of porous β-TCP scaffolds via advanced manufacturing technology. *Int. J. Mol. Sci.* **2015**, *16*, 6818–6830. [CrossRef] [PubMed]

36. Kokubo, T.; Takadama, H. How useful is SBF in predicting in vivo bone bioactivity? *Biomaterials* **2006**, *27*, 2907–2915. [CrossRef] [PubMed]